

# Explainability-Aware One Point Attack for Point Cloud Neural Networks

Hanxiao Tan    Helena Kotthaus  
AI Group, TU Dortmund

{hanxiao.tan, helena.kotthaus}@tu-dortmund.de

## Abstract

With the proposition of neural networks for point clouds, deep learning has started to shine in the field of 3D object recognition while researchers have shown an increased interest to investigate the reliability of point cloud networks by fooling them with perturbed instances. However, most studies focus on the imperceptibility or surface consistency, with humans perceiving no perturbations on the adversarial examples. This work proposes two new attack methods: one-point attack (OPA) and critical traverse attack (CTA), which go in the opposite direction: we restrict the perturbation dimensions to a human cognizable range with the help of explainability methods, which enables the working principle or decision boundary of the models to be comprehensible through the observable perturbation magnitude. Our results show that the popular point cloud networks can be deceived with almost 100% success rate by shifting only one point from the input instance. In addition, we attempt to provide a more persuasive viewpoint of comparing the robustness of point cloud models against adversarial attacks. We also show the interesting impact of different point attribution distributions on the adversarial robustness of point cloud networks. Finally, we discuss how our approaches facilitate the explainability study for point cloud networks. To the best of our knowledge, this is the first point-cloud-based adversarial approach concerning explainability. Our code is available at <https://github.com/Explain3D/Exp-One-Point-Atk-PC>.

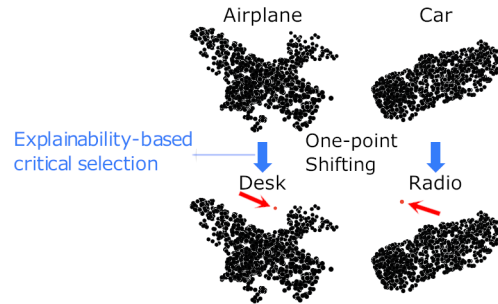


Figure 1: One point attack for point cloud networks. With the saliency map provided by the explainability method, only one point needs to be perturbed in the point set of the original instance to fool the most popular point cloud networks.

## 1 Introduction

Developments in the field of autonomous driving and robotics have heightened the need for the research of point cloud (PC) data since PCs are advantageous over other 3D representations for real-time performance. However, compared with 2D images, the robustness and reliability of PC networks have only attracted considerable attention in recent years and still not been sufficiently studied, which potentially threatens human lives e.g. driverless vehicles with point cloud recognition systems are unreliable unless they are sufficiently stable and transparent. Existing attack approaches successfully generated adversarial examples against the popular PC networks from various priorities, such as simulation of real instances [37], transferability [12], shape-consistency [17, 37] and mini-

imum perturbation distance [18, 14]. Nevertheless, despite the visually minuscule perturbation distances achieved by the methods that concentrate on imperceptibility, they still suffered from non-sparse perturbation matrixes where groups of point clusters are obligated to be shifted.

Moreover, in terms of human perception, most existing PC attack methods emphasized imperceptibility, whereby the perturbation result is sufficiently similar to the original instance that humans cannot distinguish with naked eyes. Instead, this work attempts to address the exact opposite perspective: towards a better glimpse of how the model works and its decision boundaries. We utilize explainability methods to identify the critical points that are most capable of altering the model predictions and exhibit that perturbing these key points can fool the popular PC networks with nearly 100% success rate. To the best of our knowledge, this is the first PC applicable attack approach that incorporates explainability. An example of our attack is shown in Fig. 1.

Besides, several studies set out to enhance the robustness of the model, most of them are post-hoc defense operations or external embedded modules e.g. adversarial training [18], perturbation-based examination [38] and DUP-net [42] while our work addresses unveiling the intrinsic properties of the PC networks. We discuss the robustness of different PC networks according to the experiment results, which has been attempted by previous works [38, 14, 40]. However, we argue that due to the structural differences between PCs and 2D images, a reasonable robust evaluation requires multifactorial consideration from the adversarial results.

Altogether, the contribution of this work can be summarized as follows:

- We present a new explainability perspective of PC adversarial attacks inspired by counterfactuals [4] for tabular data, with more observable prediction mechanism and decision boundaries through extremely low-dimensional points shifting.
- We propose OPA, a point cloud-applicable shifting-based attack that fools popular point cloud networks by perturbing **one point** with a high success rate.
- We propose CTA, which further improves the success rate, limits the perturbation distances and can

be easily extended to targeted attack with the cost of only few additional shifted points.

- We investigate diverse pooling architectures as alternatives of existing point cloud networks, which have an impact on the internal robustness against proposed attacks.
- We discuss a more persuasive viewpoint of evaluating the robustness of point cloud models against adversarial attacks.

The rest of the paper is organized as follows: We introduce the related researches of PC attacks in section 2, then we detailed our proposed methods in section 3. In section 4, we present the visualization of the adversarial examples and demonstrate comparative results with existing studies. In section 5 we discuss interesting observations derived from experiments with respect to robustness and explainability. We finally summarize our work in section 6.

## 2 Related Work

As the first work [31] on adversarial samples was presented, an increasing variety of attacks against 2D image neural networks followed [10, 5, 16, 24, 7, 21]. However, due to the structural distinctions with PC networks (see Supplementary section 7.1.1), we do not elaborate on the attack methods of image deep neural networks (DNN)s. Relevant information about image adversarial examples refers to [2]. It is notably that [27] investigated one-pixel attack for fooling image DNNs. However, their approach is a black-box attack based on an evolutionary algorithm, which is essentially distinct from ours.

The research on adversarial examples of PC data has come into prominence only in recent years, thus not as numerous researches has been devoted to this area as to 2D images. By extending 2D adversarial approaches to PCs, [36, 18, 38] opened up the studies of attacking PC neural networks. [12] reconstructed adversarial examples with an Auto-Encoder, which achieves preferable transferability between different PC networks. [39] investigated the isometric vulnerability of PC networks and proposed a white-box attack method via Restricted Isometry Property. [14] dedicated to the imperceptibility

of the generated adversarial examples by exploring a restricted balance between the number of perturbations and their shifting distances. [41] proposed a generative module which successfully achieves real-time targeted PC attacks. Instead of perturbing discrete points on the surface, [17] incorporated adversarial noises into the latent space of an auto-encoder to generate shape-aware attack examples. A similar shape-oriented adversarial perturbing approach was proposed by [37], which performs perturbation on the meshes to preserve the surface continuity of PCs. All the aforementioned approaches addressed the robustness of PC networks, however, we argue that both the generation process and experimental observations of the adversarial examples can be investigated in conjunction with the explainability of the PC neural networks. Note that [14, 38, 40] introduced the conception of *critical points* while generating adversarial examples, but none of them associated it with the specifically designed explainability methods such as Integrated Gradients (IG) (see equation S1 for details).

### 3 Methods

In this section, we formulate the adversarial problem in general and introduce the critical points set (subsection 3.1). We present our new attack approaches (subsection 3.2), including stopping criteria settings (subsection 3.3).

#### 3.1 Problem Statement

Let  $P \in \mathbb{R}^{n \times d}$  denotes the given point cloud instance,  $f : P \rightarrow y$  denotes the chosen PC neural network and  $M(a, b) : \mathbb{R}^{n_a \times d} \times \mathbb{R}^{n_b \times d}$  denotes the perturbation matrix between instance  $a$  and  $b$ . The goal of this work is to generate an adversarial examples  $P' \in \mathbb{R}^{n' \times d}$  which satisfies:

$$\begin{aligned} & \operatorname{argmin}(|\{m \in M(P, P') | m \neq 0\}| \\ & + \|M(P, P')\|) : f(P') \neq f(P) \end{aligned} \quad (1)$$

Note that among the three popular attack methods for PC data: point adding ( $n' > n$ ), point detaching ( $n' < n$ ) and point shifting ( $n' = n$ ), this work considers point shifting only.

We address the adversarial task in equation 1 as a gradient optimization problem. We minimize the loss on the

input PC instance while freezing all parameters of the network:

$$L = \alpha \times Z[f(P)] + \beta \times D(P, P') \quad (2)$$

where  $\alpha$  indicates the optimization rate,  $Z[f(P)]$  indicates the neuron unit corresponding to the prediction  $f(P)$  which guaranties the alteration of prediction,  $D(P, P')$  represents the quantized imperceptibility between the input  $P$  and the adversarial example  $P'$  and  $\beta$  is the distance penalizing weight. The imperceptibility has two major components, namely the perturbation magnitude and the perturbation sparsity. The perturbation magnitude can be constrained in three ways: Chamfer distance (equation S2), Hausdorff distance (equation S3) or simply Euclidean distance. We ensure perturbation sparsity by simply masking the gradient matrix, and with the help of the saliency map derived by the explainability method we only need to shift those points that contribute positively to the prediction to change the classification results, which we refer to "critical points set".

**Critical points set:** The concept was first discussed by its proposer [25], which contributes to the features of the max-pooling layer and summarizes the skeleton shape of the input objects. They demonstrated an *upper-bound* construction and proved that corruptions falling between the critical set and the upper-bound shape pose no impact on the predictions of the model. However, the robustness for critical points is not sufficiently discussed. Previous adversarial researches studied the model robustness by perturbing or dropping critical points set identified through monitoring the max-pooling layer or accumulating loss of gradients [14, 38, 40]. Nevertheless, capturing the output of the max-pooling layer struggles to identify discrepancies between key points and simultaneously, saliency maps based on raw gradients have been proved to be defective [1, 29]. We therefore introduce IG [30], the state-of-the-art gradient-based explainability approach, to further investigate the sensitivity of model robustness to the critical points set. The formulation of IG is summarized in equation S1.

#### 3.2 Attack Algorithms

**One-Point Attack (OPA):** Specifically, OPA (see Supplementary algorithm 1) is an extreme of restricting the

number of perturbed points, which requires:

$$|\{m \in M(P, P') | m \neq 0\}| = 1 \quad (3)$$

We acquire the gradients that minimize the activation unit corresponding to the original prediction, and a saliency map based on the input PC instance from the explanation generated by IG. We sort the saliency map and select the point with the top- $n$  attribution as the critical points ( $n = 1$  for OPA), and mask all points excluding the critical one on the gradients matrix according to its index. Subsequently the critical points are shifted with an iterative optimization process. An optional distance penalty term can be inserted into the optimization objective to regularize the perturbation magnitude and enhance the imperceptibility of the adversarial examples. We choose Adam [15] as the optimizer, which has been proven to perform better for optimization experiments. The optimization process may stagnate by falling into a local optimum, hence we treat every 25 steps as a recording period, and the masked Gaussian noise weighted by  $W_n$  is introduced into the perturbed points when the average of the target activation at period  $k + 1$  is greater than at period  $k$ . For the consideration of time cost, the optimization process is terminated when certain conditions are fulfilled and the attack to the current instance is deemed as a failure.

**Critical Traverse Attack (CTA):** Due to the uneven vulnerability of different PC instances, heuristically setting a uniform sparsity restriction for the critical points perturbation is challenging. CTA (pseudo-code presented in Supplementary algorithm 2) enables the perturbation sparsity constraint to be adaptive by attempting the minimum number of perturbed points for each instance subject to a successful attack. The idea of CTA is starting with the number of perturbed points  $n$  as 1 and increasing by 1 for each local failure until the prediction is successfully attacked or globally failed. Similarly, we consider the saliency map generated by IG as the selection criterion for critical points, and the alternative perturbed points are incremented from top-1 to all positively attributed points. Again, for accelerating optimization we also select Adam [15] as the optimizer. Since most PC instances can be successfully attacked by one-point shifting through the introduction of Gaussian noise in the optimization process, we discarded the noise-adding mechanism in CTA to distinguish the experiment results from

OPA. The aforementioned local failure stands for terminating the current  $n$ -points attack and starting another  $n + 1$  round, while the global failure indicates that for the current instance the attack has failed. We detail the stopping criteria for OPA and CTA in the next subsection.

### 3.3 Stopping Criteria

**OPA:** With the introduction of Gaussian random noise for OPA, the optimization process may fall into an everlasting convergence-noise addition loop, a manually configured failure threshold is therefore essential. A recorder  $R_a$  is built to record the corresponding prediction activation for each period. We set a global maximum iterations  $I_{maxg}$ . The stopping criterion of OPA is fulfilled when

$$\bullet I_{cur} > I_{maxg} \text{ or } ((Mean(R_a^{k+1}) > Mean(R_a^k) \text{ and } Var(R_a^k) \rightarrow 0)).$$

Due to the introduction of random Gaussian noise, the optimization process will not fail until the target activation has no fluctuant reaction to the Gaussian noise.

**CTA:** There are both local and global stopping criteria for CTA. Local criterion stands for terminating the current  $N_p$  perturbed points and start the  $N_p + 1$  round, which is similar with OPA. Again, we set an activation recorder  $R_a$  and a **local** maximum iterations  $I_{maxl}$ . The local stopping criterion is fulfilled when:

$$\bullet I_{cur} > I_{maxl} \text{ or } Mean(R_a^{k+1}) > Mean(R_a^k)$$

Global stopping terminates the optimization of current instance and registers it as "failed". CTA is designed to shifting all the positively attributed points  $N_{pos}$  in the worst case which is extremely time-consuming. For practical feasibility, we specify the **global** maximum iterations  $I_{maxg}$ . The global stopping criterion for CTA is fulfilled when:

$$\bullet I_{cur} > I_{maxg} \text{ or } N_p \geq N_{pos}$$

where  $N_{pos}$  is the total amount of positive attributed points according to the explanation provided by IG.

## 4 Experiments

In this section, we present and analyze the results of the proposed attack approaches. We demonstrate quantita-

tive adversarial examples in subsection 4.1 and scrutinize the qualitative result in subsection 4.2. Our experiments<sup>1</sup> were primarily conducted on PointNet [25], which in general achieves an overall accuracy of 87.1% for the classification task on ModelNet40 [35]. Moreover, we also extended our approaches to attack the most popular PC network PointNet++ [26] and DGCNN [33], which dominate the PC classification task with 90.7% and 92.2% accuracies respectively. We choose Modelnet40 [35] as the experimental dataset, which contains 12311 CAD models (9843 for training and 2468 for evaluation) from 40 common categories and is currently the most widely-applied point cloud classification data set. We randomly sampled 25 instances for each class from the test set, and then selected those instances that are correctly predicted by the model as our victim samples. For efficiency and simplicity, we initialize  $I_{maxg}$  as 2000 and 15000 for OPA and CTA respectively and  $I_{maxl}$  as 1500. Note that in this section all attacks performed are non-targeted unless specifically mentioned.

#### 4.1 Adversarial examples visualization

Fig. 2 visualizes 2 adversarial examples for OPA and CTA respectively. Note that in CTA, regardless of the absence of the restriction on the perturbation dimension, there are instances (e.g. the car in CTA) where only one-point shifting is required to generate an adversarial example. More qualitative visualizations are presented in Fig. S1 and S2.

#### 4.2 Quantitative evaluations and comparisons

In this section, we compare the imperceptibility of proposed methods with existing attacks via measuring Hausdorff and Chamfer distances as well as the number of shifted points, and demonstrate their transferability among different popular PC networks. Additionally, we show that CTA maintains a remarkably high success rate even after converting to targeted attacks.

**Imperceptibility:** We compare the quality of generated adversarial examples with other research under the

<sup>1</sup>Our code is available at <https://github.com/Explain3D/Exp-One-Point-Atk-PC>

aspect of success rate, Chamfer and Hausdorff distances, and the number of points perturbed. As table 1 shows, compared to the approaches favoring to restrict the perturbation magnitude, despite the relative laxity in controlling the distance between the adversarial examples and the input instances, our methods prevail significantly in terms of the sparsity of the perturbation matrix. Simultaneously, our methods achieve a higher success rate, implying that the network can be fooled for almost all PC instances by shifting a minuscule amount of points (even one). In the experiment, the optimization rate  $\alpha$  is empirically set to  $10^{-6}$ , which performs as the most suitable step size for PointNet after grid search. To accentuate the sparsity of the perturbation matrix, we temporarily turn off  $\beta$  to 0. Specifically for OPA, we set the Gaussian weight  $W_n$  to  $10^{-1}$ , which proved to be most suitable according to the experiments. More analytical results of different settings of  $\beta$  and  $W_n$  is demonstrated in Fig. S5.

In addition to PointNet, we also tested the performance of our proposed methods on PC networks with different architectures. Table 2 summarizes the result of attack PointNet, PointNet++ and DGCNN with both OPA and CTA respectively. Surprisingly, these state-of-the-art PC networks are vulnerable to be attacked by one point with remarkably high success rates. On the other hand, CTA achieves almost 100% success rate fooling those networks while only a single-digit number of points are shifted. Intuitively, PC neural networks appear to be more vulnerable compared to images CNNs ([27] is a roughly comparable study since they also performed one-pixel attack with the highest success rate of 71.66%) (see table S1 and Fig. S7 in supplementary for results of our OPA). An opposite conclusion has been drawn by [36], they trained the PointNet with 2D data and compared its robustness with 2D CNNs against adversarial images. Nevertheless, we argue that the adversarial examples are generated by attacking a 2D CNN, however this attack may not be aggressive for PointNet, which is specifically designed for point clouds. We will further discuss the robustness against attacks in section 5.2.

**Transferability:** We further investigate the transferability of proposed attacks across different PC networks by feeding the adversarial examples generated by one network to the others and recording the overall classification accuracy. Fig. 3 presents the adversarial transferability between PointNet, PointNet++ and DGCNN. What stands

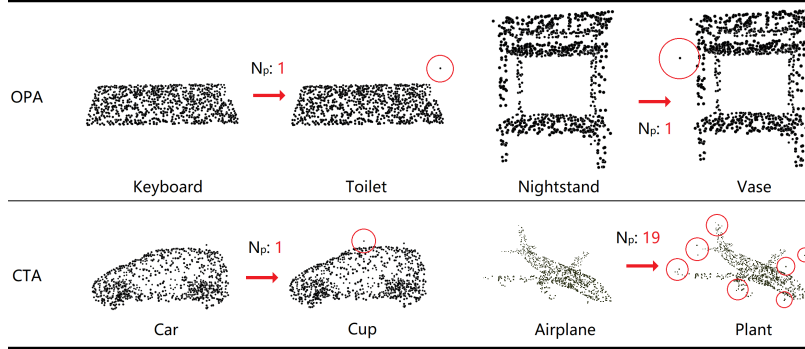


Figure 2: Adversarial examples for OPA and CTA.  $N_p$  denotes how many points are shifted.

	$S$	$D_c$	$D_h$	$N_p$
$L_p$ Norm [36]	85.9	$1.77 \times 10^{-4}$	$2.38 \times 10^{-2}$	967
Minimal selection [14]	89.4	$1.55 \times 10^{-4}$	$1.88 \times 10^{-2}$	36
Adversarial sink [19]	88.3	$7.65 \times 10^{-3}$	$1.92 \times 10^{-1}$	1024
Adversarial stick [19]	83.7	$4.93 \times 10^{-3}$	$1.49 \times 10^{-1}$	210
Random selection [34]	55.6	$7.47 \times 10^{-4}$	$2.49 \times 10^{-3}$	413
Critical selection [34]	19.0	<b><math>1.15 \times 10^{-4}</math></b>	$9.39 \times 10^{-3}$	50
Critical frequency [40]	63.2	$5.72 \times 10^{-4}$	$2.50 \times 10^{-3}$	303
Saliency map/L [40]	56.0	$6.47 \times 10^{-4}$	$2.50 \times 10^{-3}$	358
Saliency map/H [40]	58.4	$7.52 \times 10^{-4}$	<b><math>2.48 \times 10^{-3}</math></b>	424
Ours (OPA)	98.7	$8.64 \times 10^{-4}$	$8.45 \times 10^{-1}$	<b>1</b>
Ours (CTA)	<b>99.6</b>	$7.73 \times 10^{-4}$	$6.68 \times 10^{-1}$	6

Table 1: Comparison of existing point-shifting adversarial generation approaches for PointNet, where  $S$  denotes the success rate,  $D_c$  and  $D_h$  denote the Chamfer and Hausdorff distances respectively. Part of the records sourced from [14].



	Model	S	$D_c$	$D_h$	$N_p$
O	PN	98.7	$8.45 \times 10^{-4}$	$8.64 \times 10^{-1}$	1
P	PN++	<b>99.1</b>	$1.58 \times 10^{-2}$	$1.61 \times 10^1$	1
A	DGCNN	90.9	$1.70 \times 10^{-3}$	1.69	1
C	PN	<b>99.6</b>	$7.73 \times 10^{-4}$	$6.68 \times 10^{-1}$	6
T	PN++	99.5	$1.22 \times 10^{-2}$	8.90	6
A	DGCNN	100	$2.13 \times 10^{-3}$	1.48	<b>3</b>

Table 2: Comparison of attack results on PN(PointNet), PN++(PointNet++) and DGCNN.

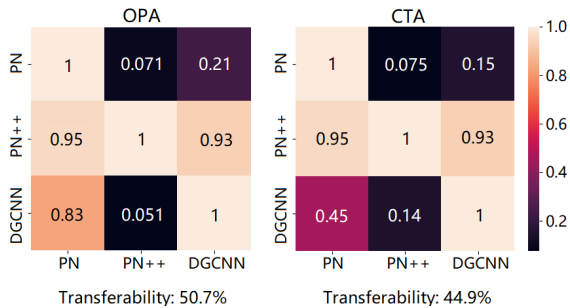


Figure 3: Transferability for PointNet, PointNet++ and DGCNN for OPA (left) and CTA (right). Networks on the rows and columns denote from which victim network the adversarial examples are generated and to which those examples are transferred respectively. Brighter squares denote higher transferabilities. The total transferabilities under the matrices are the averages of the off-diagonal values of corresponding methods.

out in the figure is that due to the aggregation of spatial adjacent points [26] and relative positional properties [33] respectively, PointNet++ and DGCNN show strong stability against the adversarial samples from PointNet. Surprisingly, PointNet++ performs stably against adversarial examples from DGCNN, while the opposite fails. Additionally, the accuracy of PointNet is severely compromised when facing the adversarial examples from the remaining two networks.

**Targeted attack:** We also attempt to extend the proposed methods to targeted attacks. To alleviate redundant experiment procedures, we employ three alternatives of conducting ergodic targeted attack: *random*, *lowest* and *second-largest* activation attack. In the random activation attack we choose one stochastic target from the 39 la-

		S	$D_c$	$D_h$	$N_p$
O	Second-largest	58.5	$9.49 \times 10^{-4}$	$9.33 \times 10^{-1}$	1
P	Random	20.9	$1.06 \times 10^{-2}$	$1.08 \times 10^1$	1
A	Lowest	6.3	$4.73 \times 10^{-3}$	4.80	1
C	Second-largest	99.5	$1.55 \times 10^{-3}$	$8.14 \times 10^{-1}$	5
T	Random	97.7	$5.75 \times 10^{-3}$	2.31	10
A	Lowest	99.0	$8.52 \times 10^{-3}$	3.06	13

Table 3: Targeted OPA and CTA on PointNet. Targeting all labels for each instance in the test set is time-consuming. Therefore, we generalize it with three substitutes: random, the second-largest and the lowest activation in the logits.

bels (excluding the ground-truth one) as the optimization destination. In the lowest and second-largest activation attack, we decrease the activation of ground truth while boosting the lowest and second-largest activation respectively until it becomes the largest one in the logits. The results, as shown in table 3, indicate that though the performance of OPA is deteriorated when converting to targeted attacks due to the rigid restriction on the perturbation dimension, while CTA survived even the worst case (lowest activation attack) with a remarkably high success rate and a minuscule number of perturbation points. As a conclusion, CTA can be converted into targeted attacks without significant compromises in success rate and the number of shifted points, at the cost of increased perturbation distance.

## 5 Discussion

In this section, we present the relevant properties of PC networks in the maximization activation experiment (5.1) as well as our viewpoint concerning the robustness of PC networks (5.2) and discuss the investigative potential of OPA for PC neural networks from the viewpoint of explainability (5.3).

### 5.1 Maximized activation

Activation Maximization (AM), first proposed by [9], sets out to visualize a global explanation of a given network through optimizing the input matrix  $x$  while freezing all parameters  $\theta$  such that the selected  $i^{th}$  activation neuron

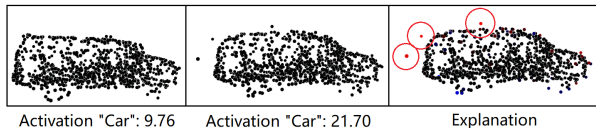


Figure 4: AM results initialized with a certain instance. The first, second and third columns demonstrate the initialized set of points, the AM output results after 1000 optimization steps and the salience map explanation of the corresponding output explained by IG, respectively. In the explanation, red points indicate the degree of positive attributions.

at  $l$  layer  $S_i^l$  is maximized [23]:

$$x^* = \operatorname{argmax}_x (a_i^l(\theta, x)) \quad (4)$$

The proposed OPA was inspired by a fruitless AM attempt for PC networks. Fig. 4 displays an examples from 1000-steps AM results of PointNet. More examples with different initializations are depicted in Fig. S8. We conduct the AM experiments with various initializations including zero, point cluster generated by averaging all test data [22] and a certain instance from the class "Car". What stands out in the visualization is that the gradient ascent of the PC neural network's activations appears to depend solely on the magnitude of the outward extension subject to the extreme individual points (the middle). We further investigate the explanations of the AM generations utilizing IG and the analysis reveals that almost all of the positive attributions are concentrated on the minority points that were expanded (the right). Fig. 5 provides a quantitative view of the trends how target activation ascends with the shifting of input points and we introduce Gini coefficient [8] to represent the "wealth gap" of the Euclidean distance among all points. Interestingly, as the target activation increments over the optimization process, the Gini coefficient of Euclidean distances steepens to 1 within few steps, indicating that the fastest upward direction of the target activation gradient corresponds with the extension of a minority of the points.

## 5.2 Reliability of PC networks

**Robustness against attacks:** Several studies have compared the robustness of existing PC networks [38, 14, 40]

through observing the performances of proposed attacks on them. In this regard, we suggest two new arguments:

*Specificity:* The observed robustness is informative only for the proposed attack method or similar ones. Notably, [14, 40] claimed that PointNet exhibits the worst robustness while [38] attributed PointNet++ as the most vulnerable one. We believe one reason is that networks differ in the sensitivity to diverse types of attacks, and thus referring to as a rich variety of attacks as possible is more appropriate when choosing a robust model.

*Absolute advantage:* In 2D images, adversarial algorithms mostly perturb the RGB or grayscale values of the pixels, which are restricted to positive numbers below 255. This property delineates an upper bound for the perturbation distance of a single pixel, the overall perturbation distance can be upper-limit estimated by counting the number of perturbed pixels, which establishes a certain correlation between perturbation sparsity and the overall perturbation distance. However, the values in PC data represent locational information of the spatial coordinate system, which has no numerical limitations. This specificity leads to the independence of the sparsity and overall distance of perturbations and complicates the robust comparison of PC models. We argue that a reasonable comparison requires simultaneous consideration of three dimensions, i.e. attack success rate, perturbation sparsity, and overall (or average) shifting distance. In an ideal scenario, e.g. the results from [14], DGCNN shows the domination with the lowest attack success rate, highest shifting distance and most perturbed points. Nevertheless, such a perfect occurrence happens infrequently. Table 1 presents an example where domination is almost nonexistent (here we compare the attack performances against the same model): Critical selection [34] dominates with the minimum  $D_c$  and a competitive  $N_p$  (less than 5%) while its success rate is incompetent, our OPA achieves satisfactory success rate with least  $N_p$  while the restriction of shifting distance is weakened, thus an arbitrary quality judgment of those approaches is unreasonable. Towards better fairness, we suggest that excluding those dimensions where a model has unidirectional advantages, values in the remaining dimensions of competitors should be identical or comparable.

From the aforementioned perspective, OPA sheds a light on the robustness of popular PC models against **critical point perturbation**. As can be seen from the table



	Acc.	S	$D_c$	$D_h$	$N_{pos}$	Gini.
Max-pooling	87.1	98.7	$8.45 \times 10^{-4}$	$8.64 \times 10^{-1}$	397.2	0.91
Average-pooling	83.8	44.8	$2.94 \times 10^{-3}$	2.96	718.5	0.53
Median-pooling	74.5	0.9	$1.28 \times 10^{-4}$	$9.55 \times 10^{-2}$	548.1	0.57
Sum-pooling	76.7	16.7	$2.50 \times 10^{-3}$	2.53	868.2	0.49

Table 4: Model accuracies, success attacking rates, average Chamfer and Hausdorff distances of OPA on PointNet with max, average, median and sum-pooling on the last layer respectively. The evaluation accuracy is also presented in the second column.  $N_{pos}$  denotes how many points are positively attributed to the prediction, and Gini. denotes the Gini coefficient of the corresponding attribution distributions.

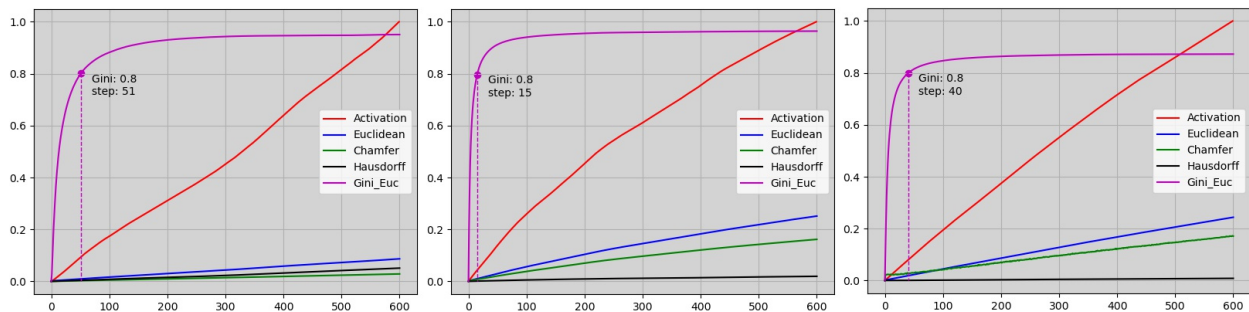


Figure 5: Correlation between the ascending target activation and the various distances of the optimized example from the original initializations: zero (left), the average of the test set (middle) and a certain instance (right). Activations are normalized in order to be visible together with other factors. X-axis denotes the optimization steps and y-axis denotes corresponding values in the legend. The marked points are the steps in the optimization process where the Gini coefficient of the attribution first reaches 0.8.

2, OPA achieves a comparable success rate for all models while the number of shifting points remains consistently 1. Then we found that PointNet is considered to be most vulnerable to critical-points shifting due to the lowest requested  $D_c$  and  $D_h$ . Oppositely, the required  $H_c$  and  $H_d$  for attacking PointNet++ are almost ten times as DGCNN, leading to the conclusion that PointNet++ appears to have the best critical-points stability. Note that our robustness conclusions are only regarding critical point perturbation, depending on the adversarial methods different conclusions may be drawn, and we are looking forward to furthering relevant discussions.

**Structural stability:** Plenty of researches have discussed defense strategies against intentional attacks for PC networks [38, 18, 42, 19, 14, 28, 41, 37], the majority of these studies were with respect to embedded defense modules, such as outlier removal. However, there has been little discussion about the stability of the intrinsic ar-

chitectures for PC networks. Inspired by the experiments of [28] who investigated the impacts of different pooling layers on the robustness, we attempt to replace the max-pooling in PointNet with multifarious pooling layers. As table 4 shows, although PointNet with average and sum-pooling sacrifice 3.3% and 10.4% accuracies in the classification task of the test set, the success rates of OPA on them plummet from 98.7% to 44.8% and 16.7% respectively, and the requested perturbation magnitudes are dramatically increased, which stands for enhanced stabilization. We speculate that it depends on how many points from the input instances the model employs as bases for predictions. As a verification, we calculate the normalized IG contributions of all points from the instances correctly predicted among the 2468 test instances, and we also introduce the Gini coefficient [8] to quantify the dispersion of the absolute attributions which is formulated as:

$$G = \frac{\sum_{i=1}^n \sum_{j=1}^n ||a_i| - |a_j||}{2n^2 |\bar{a}|} \quad (5)$$

where  $a$  is the attribution mask generated by IG. We demonstrate the corresponding results in table 4, 5 and Fig. S9. There are significant distributional distinctions between the max, average and sum-pooling architectures. PointNet with average and sum-poolings adopt 70.18% (718.5 points) and 84.78% (868.2 points) of the points to positively sustain the corresponding predictions, where the percentages of points attributed to the top 20% are 0.65% (6.7 points) and 1.16% (11.9 points), respectively, while these proportions are only 38.79% (397.2 points) and 0.15% (1.5 points) in the max-pooling structured PointNet. Moreover, the Gini coefficients reveal that in comparison to the more even distribution of attributions in average (0.53) and sum-pooling (0.49), the dominant majority of attributions in PointNet with max-pooling are concentrated in a minuscule number of points (0.91). Hence, it could conceivably be hypothesized that for PC networks, involving and apportioning the attribution across more points in prediction would somewhat alleviate the impact of corruption at individual points on decision outcomes, and thus facilitate the robustness of the networks. Surprisingly, median-pooling appears to be an exception. While the success rate of OPA is as low as 0.9%, the generated adversarial examples only require perturbing  $9.55 \times 10^{-2}$  of the Hausdorff distance in average (all experiments sharing the same parameters, i.e. without any distance penalty attached). On the other hand, despite that merely 53.53% (548.1) points are positively attributed to the corresponding predictions, with only 0.23% (2.4 points) of them belonging to the top 20%, which is significantly lower than the average and sum-pooling architectures, median-pooling is almost completely immune to the deception of OPA. We believe that median-pooling is insensitive to extreme values, therefore the stability to perturbations of a single point is dramatically reinforced.

### 5.3 Towards explainable PC models

Despite the massive number of adversarial methods that have made significant contributions to the studies of model robustness for computer vision tasks, to our best

	Top 20%	Top 40%	Positive
Max-pooling	0.15%	0.23%	38.79%
Average-pooling	0.65%	2.12%	70.18%
Median-pooling	0.23%	0.59%	53.53%
Sum-pooling	1.16%	4.53%	84.78%

Table 5: Overview of the percentage of top-20%, top-40% and positive attributed points with four different pooling layers. Complete pie diagrams are shown in Fig. S9.

knowledge, no adversarial research has discussed the explainability of **PC networks**. However, we believe that the adversarial methods can facilitate the explainability of the model to some extent. Recall the roles of counterfactuals in investigating the explainability of models processing tabular data [4]. Counterfactuals provide explanations for chosen decisions by describing what changes on the input would lead to an alternative prediction while minimizing the magnitude of the changes to preserve the fidelity, which is identical to the process of generating adversarial examples [6]. Unfortunately, owing to the multidimensional geometric information that is unacceptable to the human brain, existing image-oriented approaches addressed the counterfactual explanations only at the semantic level [11, 32].

Several studies have documented that a better explanatory counterfactual needs to be sparse because of the limitations on human category learning [13] and working memory [20, 3]. Therefore we argue that unidimensional perturbations contribute to depicting relatively perceptible decision boundaries. Fig. 6 compares the visualization of multidimensional and unidimensional perturbations. The unidimensional shift, though larger in magnitude, shows more clearly the perturbation process of the prediction from "car" to "radio", and makes it easier to perceive the decision boundary of the model. Conversely, while higher dimensional perturbations perform better on imperceptibility for humans, they are more difficult for understanding the shifting principles or decision boundary of the model.

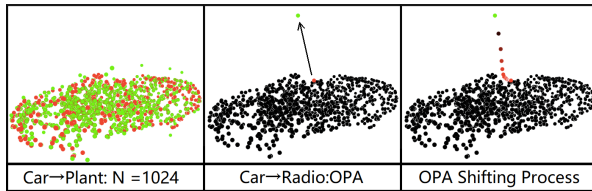


Figure 6: Intuitive visualization of multidimensional shifting(left), unidimensional OPA shifting(middle) and the shifting process of OPA. The redder the point the higher the prediction score for the label "car". Green points denote the shifting destinations.

## 6 Conclusion

As the first attack method for PC networks incorporating explainability, we proposed two attack approaches with extreme low-dimensional shifting on the most popular PC networks. We exhibited that most PC networks are susceptible to perturbations at critical points. We discussed our viewpoints while evaluating the robustness of PC networks as well as their explainability. In future investigations, it might be possible to distill existing PC networks according to the critical points into more explainable architectures. Besides, we are looking forward to higher-quality and human-understandable explanations for PC networks.

## References

- [1] Julius Adebayo, Justin Gilmer, Michael Muelly, Ian Goodfellow, Moritz Hardt, and Been Kim. Sanity checks for saliency maps. *arXiv preprint arXiv:1810.03292*, 2018. [3](#)
- [2] Naveed Akhtar and Ajmal Mian. Threat of adversarial attacks on deep learning in computer vision: A survey. *Ieee Access*, 6:14410–14430, 2018. [2](#)
- [3] George A Alvarez and Patrick Cavanagh. The capacity of visual short-term memory is set both by visual information load and by number of objects. *Psychological science*, 15(2):106–111, 2004. [10](#)
- [4] Ruth MJ Byrne. Counterfactuals in explainable artificial intelligence (xai): Evidence from human reasoning. In *IJ-CAI*, pages 6276–6282, 2019. [2](#), [10](#)
- [5] Nicholas Carlini and David Wagner. Towards evaluating the robustness of neural networks. In *2017 IEEE Symposium on Security and Privacy (SP)*, pages 39–57. IEEE, 2017. [2](#)
- [6] Susanne Dandl, Christoph Molnar, Martin Binder, and Bernd Bischl. Multi-objective counterfactual explanations. In *International Conference on Parallel Problem Solving from Nature*, pages 448–469. Springer, 2020. [10](#)
- [7] Yinpeng Dong, Fangzhou Liao, Tianyu Pang, Hang Su, Jun Zhu, Xiaolin Hu, and Jianguo Li. Boosting adversarial attacks with momentum. In *Proceedings of the IEEE conference on computer vision and pattern recognition*, pages 9185–9193, 2018. [2](#)
- [8] Robert Dorfman. A formula for the gini coefficient. *The review of economics and statistics*, pages 146–149, 1979. [8](#), [9](#)
- [9] Dumitru Erhan, Yoshua Bengio, Aaron Courville, and Pascal Vincent. Visualizing higher-layer features of a deep network. *University of Montreal*, 1341(3):1, 2009. [7](#)
- [10] Ian J Goodfellow, Jonathon Shlens, and Christian Szegedy. Explaining and harnessing adversarial examples. *arXiv preprint arXiv:1412.6572*, 2014. [2](#)
- [11] Yash Goyal, Ziyang Wu, Jan Ernst, Dhruv Batra, Devi Parikh, and Stefan Lee. Counterfactual visual explanations. In *International Conference on Machine Learning*, pages 2376–2384. PMLR, 2019. [10](#)
- [12] Abdullah Hamdi, Sara Rojas, Ali Thabet, and Bernard Ghanem. Advpc: Transferable adversarial perturbations on 3d point clouds. In *European Conference on Computer Vision*, pages 241–257. Springer, 2020. [1](#), [2](#)
- [13] Mark T Keane and Barry Smyth. Good counterfactuals and where to find them: A case-based technique for generating counterfactuals for explainable ai (xai). In *International Conference on Case-Based Reasoning*, pages 163–178. Springer, 2020. [10](#)
- [14] Jaeyeon Kim, Binh-Son Hua, Duc Thanh Nguyen, and Sai-Kit Yeung. Minimal adversarial examples for deep learning on 3d point clouds. *arXiv preprint arXiv:2008.12066*, 2020. [2](#), [3](#), [6](#), [8](#), [9](#), [14](#)
- [15] Diederik P Kingma and Jimmy Ba. Adam: A method for stochastic optimization. *arXiv preprint arXiv:1412.6980*, 2014. [4](#)
- [16] Alexey Kurakin, Ian Goodfellow, Samy Bengio, et al. Adversarial examples in the physical world, 2016. [2](#)
- [17] Kibok Lee, Zhuoyuan Chen, Xinchen Yan, Raquel Urtasun, and Ersin Yumer. Shapeadv: Generating shape-aware adversarial 3d point clouds. *arXiv preprint arXiv:2005.11626*, 2020. [1](#), [3](#), [14](#)
- [18] Daniel Liu, Ronald Yu, and Hao Su. Extending adversarial attacks and defenses to deep 3d point cloud classifiers. In *2019 IEEE International Conference on Image Processing (ICIP)*, pages 2279–2283. IEEE, 2019. [2](#), [9](#)
- [19] Daniel Liu, Ronald Yu, and Hao Su. Adversarial shape perturbations on 3d point clouds. In *European Conference on Computer Vision*, pages 88–104. Springer, 2020. [6](#), [9](#), [14](#)
- [20] George A Miller. The magical number seven, plus or minus two: Some limits on our capacity for processing information. *Psychological review*, 63(2):81, 1956. [10](#)
- [21] Seyed-Mohsen Moosavi-Dezfooli, Alhussein Fawzi, and Pascal Frossard. Deepfool: a simple and accurate method to fool deep neural networks. In *Proceedings of the IEEE conference on computer vision and pattern recognition*, pages 2574–2582, 2016. [2](#)
- [22] Anh Nguyen, Jason Yosinski, and Jeff Clune. Multifaceted feature visualization: Uncovering the different types of features learned by each neuron in deep neural networks. *arXiv preprint arXiv:1602.03616*, 2016. [8](#), [22](#)
- [23] Anh Nguyen, Jason Yosinski, and Jeff Clune. Understanding neural networks via feature visualization: A survey. In *Explainable AI: interpreting, explaining and visualizing deep learning*, pages 55–76. Springer, 2019. [8](#)
- [24] Nicolas Papernot, Patrick McDaniel, Ian Goodfellow, Somesh Jha, Z Berkay Celik, and Ananthram Swami. Practical black-box attacks against machine learning. In *Proceedings of the 2017 ACM on Asia conference on computer and communications security*, pages 506–519, 2017. [2](#)
- [25] Charles R Qi, Hao Su, Kaichun Mo, and Leonidas J Guibas. Pointnet: Deep learning on point sets for 3d classification and segmentation. In *Proceedings of the IEEE conference on computer vision and pattern recognition*, pages 652–660, 2017. [3](#), [5](#), [14](#)
- [26] Charles R Qi, Li Yi, Hao Su, and Leonidas J Guibas. Pointnet++: Deep hierarchical feature learning on point sets in

- a metric space. *arXiv preprint arXiv:1706.02413*, 2017. 5, 7, 14
- [27] Jiawei Su, Danilo Vasconcellos Vargas, and Kouichi Sakurai. One pixel attack for fooling deep neural networks. *IEEE Transactions on Evolutionary Computation*, 23(5):828–841, 2019. 2, 5
- [28] Jiachen Sun, Karl Koenig, Yulong Cao, Qi Alfred Chen, and Z Morley Mao. On the adversarial robustness of 3d point cloud classification. *arXiv preprint arXiv:2011.11922*, 2020. 9
- [29] Mukund Sundararajan, Ankur Taly, and Qiqi Yan. Gradients of counterfactuals. *arXiv preprint arXiv:1611.02639*, 2016. 3, 14
- [30] Mukund Sundararajan, Ankur Taly, and Qiqi Yan. Axiomatic attribution for deep networks. In *International Conference on Machine Learning*, pages 3319–3328. PMLR, 2017. 3, 14
- [31] Christian Szegedy, Wojciech Zaremba, Ilya Sutskever, Joan Bruna, Dumitru Erhan, Ian Goodfellow, and Rob Fergus. Intriguing properties of neural networks. *arXiv preprint arXiv:1312.6199*, 2013. 2
- [32] Tom Vermeire and David Martens. Explainable image classification with evidence counterfactual. *arXiv preprint arXiv:2004.07511*, 2020. 10
- [33] Yue Wang, Yongbin Sun, Ziwei Liu, Sanjay E Sarma, Michael M Bronstein, and Justin M Solomon. Dynamic graph cnn for learning on point clouds. *Acm Transactions On Graphics (tog)*, 38(5):1–12, 2019. 5, 7, 14
- [34] Matthew Wicker and Marta Kwiatkowska. Robustness of 3d deep learning in an adversarial setting. In *Proceedings of the IEEE/CVF Conference on Computer Vision and Pattern Recognition*, pages 11767–11775, 2019. 6, 8
- [35] Zhirong Wu, Shuran Song, Aditya Khosla, Fisher Yu, Linguang Zhang, Xiaoou Tang, and Jianxiong Xiao. 3d shapenets: A deep representation for volumetric shapes. In *Proceedings of the IEEE conference on computer vision and pattern recognition*, pages 1912–1920, 2015. 5, 14
- [36] Chong Xiang, Charles R Qi, and Bo Li. Generating 3d adversarial point clouds. In *Proceedings of the IEEE/CVF Conference on Computer Vision and Pattern Recognition*, pages 9136–9144, 2019. 2, 5, 6, 14
- [37] Jinlai Zhang, Lyujie Chen, Binbin Liu, Bo Ouyang, Qizhi Xie, Jihong Zhu, and Yanmei Meng. 3d adversarial attacks beyond point cloud. *arXiv preprint arXiv:2104.12146*, 2021. 1, 3, 9, 14
- [38] Qiang Zhang, Jiancheng Yang, Rongyao Fang, Bingbing Ni, Jinxian Liu, and Qi Tian. Adversarial attack and defense on point sets. *arXiv preprint arXiv:1902.10899*, 2019. 2, 3, 8, 9, 14
- [39] Yue Zhao, Yuwei Wu, Caihua Chen, and Andrew Lim. On isometry robustness of deep 3d point cloud models under adversarial attacks. In *Proceedings of the IEEE/CVF Conference on Computer Vision and Pattern Recognition*, pages 1201–1210, 2020. 2
- [40] Tianhang Zheng, Changyou Chen, Junsong Yuan, Bo Li, and Kui Ren. Pointcloud saliency maps. In *Proceedings of the IEEE/CVF International Conference on Computer Vision*, pages 1598–1606, 2019. 2, 3, 6, 8
- [41] Hang Zhou, Dongdong Chen, Jing Liao, Kejiang Chen, Xiaoyi Dong, Kunlin Liu, Weiming Zhang, Gang Hua, and Nenghai Yu. Lg-gan: Label guided adversarial network for flexible targeted attack of point cloud based deep networks. In *Proceedings of the IEEE/CVF Conference on Computer Vision and Pattern Recognition*, pages 10356–10365, 2020. 3, 9, 14
- [42] Hang Zhou, Kejiang Chen, Weiming Zhang, Han Fang, Wenbo Zhou, and Nenghai Yu. Dup-net: Denoiser and upsampler network for 3d adversarial point clouds defense. In *Proceedings of the IEEE/CVF International Conference on Computer Vision*, pages 1961–1970, 2019. 2, 9, 14



## 7 Supplementary Material

This section is a supplement for the main part of the paper. In this section, we detail additional formulas for the backgrounds (7.1), demonstrate our Pseudo-codes (7.2), show more adversarial examples for both OPA and CTA respectively (7.3), visualize the diversity of attacking labels (7.4), discuss the most appropriate hyper-parameter settings (7.5). We also present the attack result OPA on 2D images as a comparable reference (7.6). Finally, we provide more visualisations of the Activation Maximization (AM) and the attribution distribution of PC networks (7.7 and 7.8 respectively.)

### 7.1 Background

#### 7.1.1 Point cloud deep neural networks

A PC input can be represented as  $P = \{p_0, \dots, p_n\}$ , where  $p_i \in \mathbb{R}^3$  and  $n$  is the number of component points. Compared with 2D images, the structural peculiarity of PC data lies in the irregularity: let  $R(S)$  be a function that randomly disrupts the order of the sequence  $S$ , a PC classifier  $f$  must possess such properties:  $f(P) = f(R(P))$ , which is regarded as a "symmetric system". The pioneer of PC networks is proposed by [25], succeeded by employing an symmetric function  $g(S)$  and an element-wise transformer  $h(p)$  where  $f(P) \approx g(\{h(p_0), \dots, h(p_n)\})$  (in their experiments a max-pooling is chosen as  $g(S)$ ). PointNet++ [26], the successor of PointNet, further coalesced hierarchical structures by introducing spatial adjacency via grouping of nearest-neighbors. DGCNN [33] extended the the predecessors by dynamically incorporating graph relationships between multiple layers. All of the point-based methods achieve satisfactory accuracies on acknowledged PC dataset such as ModelNet40 [35].

#### 7.1.2 Integrated Gradients

Gradients-based explainability methods are oriented on generating saliency maps of inputs by calculating gradients during propagation. While vanilla gradients severely suffer from attribution saturation [29], [30] proposes IG which accumulates attributions from an appropriate baseline before the gradients reach the saturation threshold. IG is formulated as:

$$IG_i = (x_i - x'_i) \cdot \int_{\alpha=0}^1 \frac{\partial F(x' + \alpha(x - x'))}{\partial x} d\alpha \quad (S1)$$

Where  $x'$  denotes the given baseline.

#### 7.1.3 Similarity measurement for point cloud data

Due to the irregularity of PCs, Manhattan and Euclidean distance are both no longer applicable when measuring the similarity between PC instances. Several previous works introduce Chamfer [14, 38, 36, 17, 19, 41, 37] and Hausdorff [42, 14, 38, 36, 19, 41] distances to represent the imperceptibility of adversarial examples. The measurements are formulated as:

- Bidirectional Chamfer distance

$$D_c(P_a, P_b) = \frac{1}{|P_a|} \sum_{p_m \in P_a} \min_{p_n \in P_b} \|p_m - p_n\|_2 + \frac{1}{|P_b|} \sum_{p_n \in P_b} \min_{p_m \in P_a} \|p_n - p_m\|_2 \quad (S2)$$

- Bidirectional Hausdorff distance

$$D_h(P_a, P_b) = \max(\max(\min_{p_n \in P_b} \|p_m - p_n\|_2), \max(\min_{p_m \in P_a} \|p_n - p_m\|_2)) \quad (S3)$$

#### 7.1.4 Targeted vs. Untargeted attack

For a given classifier  $f$  and its logits  $a$ , an PC input instance  $P$  and an adversarial perturbation  $A_p$ :

- Targeted attack

$$\text{Minimize } (a[f(P)+A_p]) \quad \text{s.t. } f(P+A_p) \neq f(P) \quad (S4)$$

- Untargeted attack

$$\text{Maximize } (a[f(P+A_p)]) \quad \text{s.t. } f(P+A_p) = T \quad (S5)$$

Where  $T$  is the given target class.

## 7.2 Pseudo-codes of glsopa and glseta

In this section we present the Pseudo-codes for both OPA and CTA as a supplement for section 3.2.

## 7.3 More qualitative visualizations for OPA and CTA

We selected 10 representative classes from Modelnet40 that occur most frequently in the real world and demonstrate another 10 adversarial examples for each class generated by OPA and CTA in Fig. S1 and S2 respectively. The perturbed points are colored with red for better visualization. As the success rate of the OPA attack is close to 100%, in order to distinguish the results of CTA from OPA more clearly, we set  $\beta$  in CTA as  $(8 \times \alpha)$ . This setting makes a good trade-off between success rate, shifting distance and perturbation dimensionality. The detailed experimental results are demonstrated in section 7.5.

## 7.4 Label Diversity of adversarial examples

For non-targeted OPA and CTA, the optimization process diminishes the neurons corresponding to the original labels, with no interest in the predicted labels of the adversarial examples. However, we found that observing the adversarial labels helped to understand the particularities of the adversarial examples. Fig. S3 and S4 report the label distribution matrices of untargeted OPA and CTA respectively. As can be seen from Fig. S3, class "radio" is most likely to be the adversarial label, and most of the adversarial examples generated within the same class are concentrated in one of the other categories (e.g. almost all instances from "door" are optimized towards "curtain"). This phenomenon is significantly ameliorated in CTA (see Fig. S4). The target labels are more evenly distributed in the target label matrix, yielding more diversity in the adversarial examples.

## 7.5 Hyper-parameter settings

### 7.5.1 Distance regularization $\beta$

For both proposed algorithms, there are two crucial hyper-parameters to be tuned that affect the performance of the attacks, i.e.  $\alpha$  and  $\beta$ .  $\alpha$  indicates the optimization rate

---

**Algorithm 1:** N-critical points attack. ( $n = 1$  for OPA)

---

**Input:**  $P \rightarrow N \times D$  PC data,  $f \rightarrow$  PC neural network,  $\alpha \rightarrow$  Optimizing rate,  $\beta \rightarrow$  Weight for constrain the perturbing distance(optional),  $D \rightarrow$  Distance calculating function(optional),  $N_p \rightarrow$  Number of shifting points(1 for *One-point attack*),  $W_n \rightarrow$  Gaussian noise weights

**Output:**  $P_{adv} \rightarrow N \times D$  Adversarial example

```

1  $A_{idx} = \text{Argsort}(IG(P, f))$  // Get IG mask of P
2  $R_s = \text{list}()$  // Activation Recorder
3  $I_{cur} = 1$  // Current iteration
4 while True do
5    $a_p \leftarrow f(P)$  // Current activation of predicted class
6    $G = \alpha * A_p + \beta * D(P_{adv}, P)$  // Add distance constrain(Optional)
7    $P_{adv} = \text{Adam}(P_{adv}, G[A_{idx}[1 : N]])$  // Adam optimizing N points
8    $I_{cur} += 1$ 
9    $R_s.append(a_p)$ 
10  /* Add masked Gaussian random noise if activation descending stopped */
11  if  $R_s[t] < R_s[t + 1]$  then
12     $P_{adv} += W_n \times \text{GaussianRandom}(P_\delta)[A_{idx}[1 : N]]$ 
13    /* Success if predict class changed */
14    if  $\max(a) \neq \text{pred}$  then
15      return  $P_{adv}$ 
16    /* Fails if the stopping conditions related to  $R_a$  and  $I_{cur}$  are fulfilled */
17  if Stopping criteria are fulfilled then
18    return Failed

```

---



Figure S1: More results from OPA. We chose the 10 representative classes that appear more frequently in the real world. The perturbed points are indicated in red to be noticeable.



Figure S2: More results from CTA. We also chose the 10 representative classes that appear more frequently in the real world. The perturbed points are indicated in red to be noticeable.

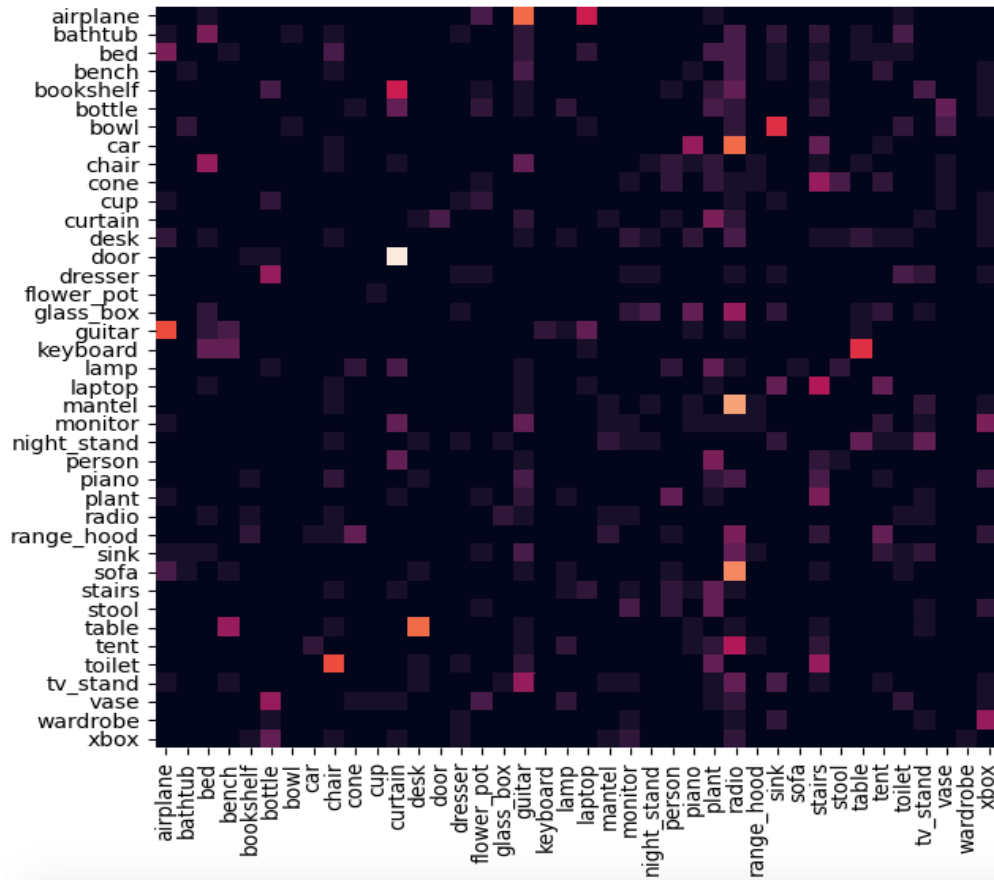


Figure S3: Heat map of successful attacks by OPA across labels. Rows indicate from which category the adversarial examples come and the columns indicate to which category they are predicted. The brighter the square, the more examples that fall into the corresponding category.



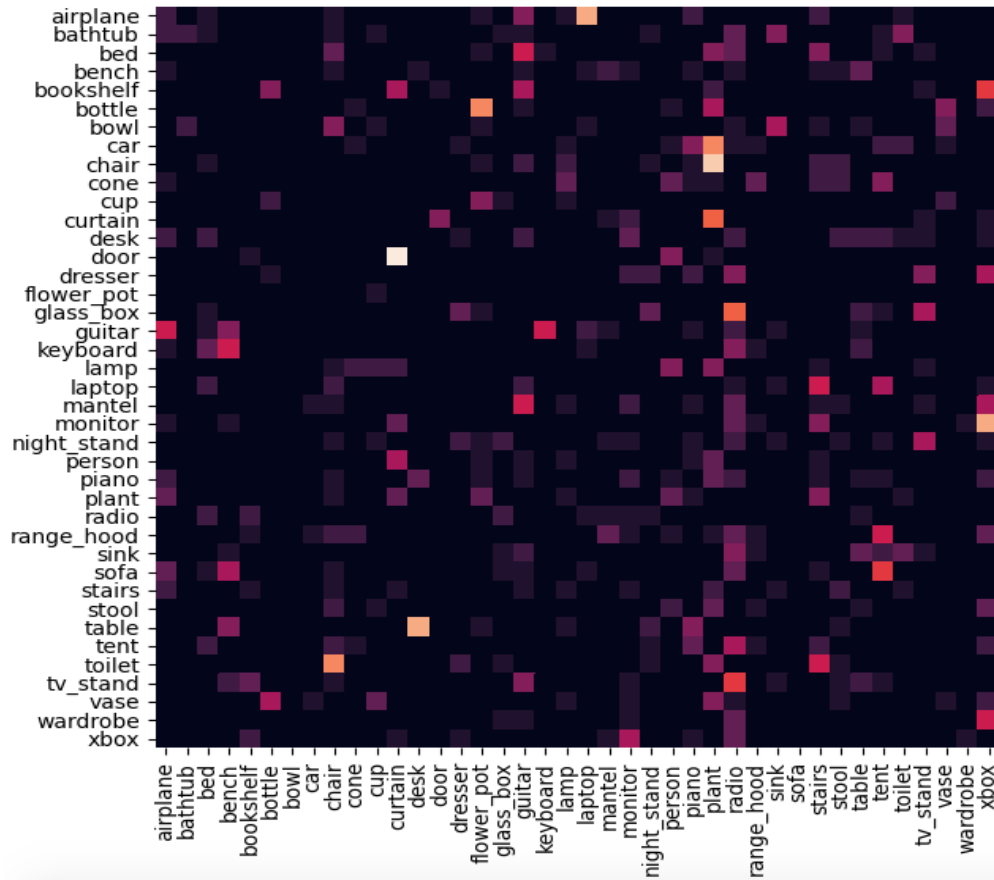


Figure S4: Heat map of successful attacks by CTA across labels. Rows indicate from which category the adversarial examples come and the columns indicate to which category they are predicted. The brighter the square, the more examples that fall into the corresponding category.

---

**Algorithm 2:** Critical traverse attack (CTA)

---

**Input:**  $P \rightarrow N \times D$  PC data,  $f \rightarrow$  PC neural network,  $\alpha \rightarrow$  Optimizing rate,  $\beta \rightarrow$  Weight for constrain the perturbing distance(optional),  $D \rightarrow$  Distance measuring function(optional)

**Output:**  $P_{adv} \rightarrow N \times D$  Adversarial example

```
1  $A_{idx} = \text{Argsort}(IG(P, f))$  // Get IG mask of P
2  $Num_{pos} = \text{count}(IG(P, f) > 0)$  // # Points with attribution >0
3  $R_s = \text{list}()$ 
4  $I_{cur} = 1$ 
5 for  $N_p$  from 1 to  $Num_{pos}$  do
6   while True do
7      $a_p \leftarrow f(P)$  // Activation of predicted class
8      $G = \alpha * A_p + \beta * D(P_{adv}, P)$  // Add distance constrain(Optional)
9      $P_{adv} = \text{Adam}(P_{adv}, G[A_{idx}[1 : N_p]])$ 
10    // Adam optimizing N points
11     $I_{cur} += 1$ 
12     $R_s.append(a_p)$ 
13    /* Success if predict class changed */
14    if  $\text{argmax}(a_p) \neq \text{pred}$  then
15       $\_return P_{adv}$ 
16    /* Current  $N_p$  round fails if the local stopping conditions related to  $R_a$  and  $I_{cur}$  are fulfilled */
17    if Local stopping criteria fulfilled then
18       $\_break;$ 
19    /* Current instance fails if the global stopping conditions are fulfilled */
20    if Global stopping criteria fulfilled then
21       $\_return Failed$ 
22   $\_return Failed$ 
```

---

and is empirically set to  $1e - 6$ .  $\beta$  indicates the penalty of perturbation distances, which regularizes the shifting magnitude and preserves the imperceptibility of adversarial examples. In previous experiments, we temporarily set  $\beta$  to 0 to highlight the sparse perturbation dimensions. However, additional investigations suggest that appropriate  $\beta$  can further improve the performance of the proposed approaches. Fig. S5 demonstrates the performances with different  $\beta$  settings. Interestingly, we found that CTA performs best when  $\beta = \alpha$ : while maintaining nearly 100% success rate and comparably shifting distances, its average  $N_p$  dramatically decreases to 3.04 (different from OPA, CTA employs no random-noise). We strongly recommend restricting  $\beta$  to a reasonable range ( $\leq (8 \times \alpha)$ ) since large  $\beta$  easily leads to an explosion in processing time.

### 7.5.2 Gaussian noise weight $W_n$ for OPA

In particular for OPA, another hyperparameter  $W_n$  is set to prevent the optimization process from stagnating at a local optimum. We experimented with various settings of  $W_n$  and present the results in Fig. S6. What stands out in the figure is that the appropriate range for  $W_n$  is around  $10^{-1}$  to  $10^{-0.5}$  where the success rate approximates 100% while maintaining acceptable perturbation distances. Adding Gaussian noise in the optimization process dramatically enhances the attack performance of OPA, with its success rate increasing from 56.1% as a simple-gradient attack to almost 100%. Interestingly, we observe that a suitable noise weight concurrently reduces the perturbation distance and thus augments the imperceptibility of the adversarial examples. We attribute this to the promotion of Gaussian noise that facilitates the optimizer to escape from saddle planes or local optimums faster, reducing the number of total iterations. However, overweighting deviates the critical point from the original optimization path, which is equivalent to resetting another starting position in 3D space and forcing the optimizer to start iterating again. While there remains a high probability of finding an adversarial example, its imperceptibility is severely impaired.

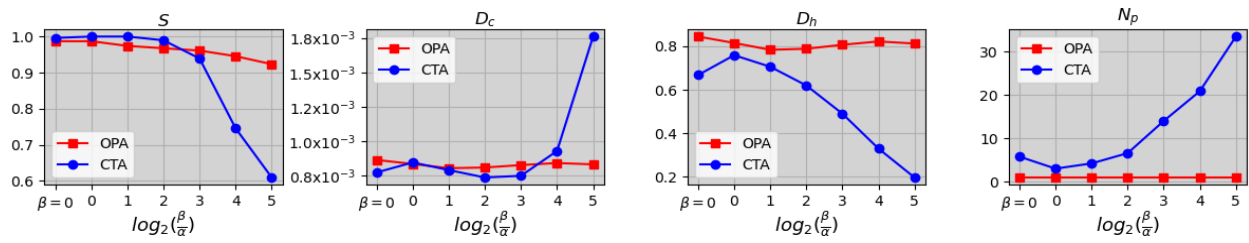


Figure S5: Performance (success rate, Chamfer and Hausdorff distances and the number of shifted points respectively) of OPA and CTA in different settings of hyper-parameters. The x-axis indicates the logarithm of the quotient of  $\beta$  and  $\alpha$  where the first tick denotes  $\beta = 0$ .

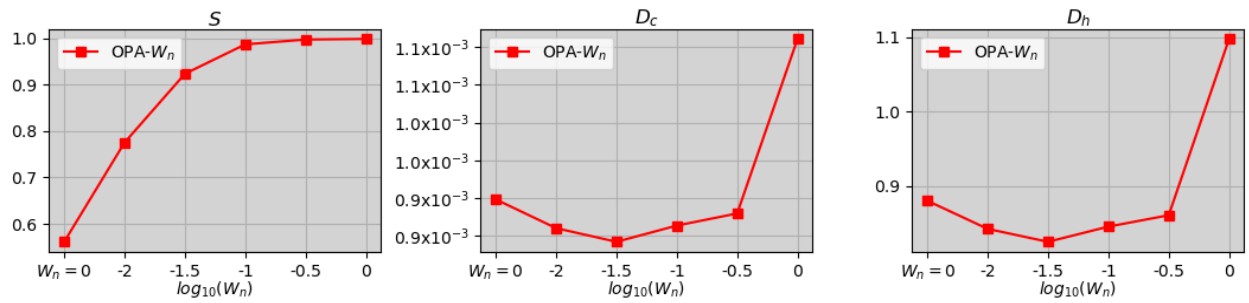


Figure S6: Performance (success rate, Chamfer and Hausdorff distances respectively) of OPA in different settings of weights for Gaussian noise. The x-axis indicates the logarithm of  $W_n$  where the first tick denotes  $W_n = 0$ .

## 7.6 OPA on 2D image neural network

For a relatively fair comparison as a reference, we extend our OPA to 2D image neural networks for a rough comparison of its sensitivity to critical points with that of 3D networks. We trained a simple ResNet18 network with the MNIST handwriting dataset, which achieves an accuracy of 99% on the test set. We select 1000 samples from the test set as victims to be attacked with OPA. The quantitative results and parts of the adversarial examples are demonstrated in table S1 and Fig. S7 respectively. In Fig. S7, the original instances and their adversarial results are listed on the first and the second row respectively. With the removal of a pixel in a critical location, a small number of test images successfully fooled the neural network. However from a quantitative viewpoint (table S1), shifting one critical point almost fails to fool the ResNet18 network (1.2% success rate for ResNet18-GR). We believe the reasons are: (1) 2D images are restricted within the RGB/greyscale space, thus there exists an upper bound on the magnitude of the perturbation, while 3D point clouds are infinitely extendable; (2) Large-size convolutional kernels ( $\geq 2$ ) learn local features of multiple pixels, which mitigates the impact of individual points on the overall prediction. According to observation (1), we temporarily remove the physical limitation during attacks to investigate the pure mechanism inside both networks and report the results in ResNet18-GF of table S1. Though the attack success rate climbs to 51.7%, there is still a gap with PointNet (98.7%). PointNet encodes points with  $1 \times 1$  convolutional kernels, which is analogous to an independent weighting process for each point. The network inclines to assign a large weight to individual points due to the weak local correlation of adjacent points and therefore leads to vulnerable robustness against perturbations of critical points.

## 7.7 Additional Activation Maximization (AM) results

For fairness and persuasion, we conduct AM experiments with various initializations as a supplement of section 5.1. Fig. S8 shows AM initialized with zeros and the point cluster generated by averaging all test data [22].

	S	$D_c$	$D_h$
ResNet18-GR	1.2	$4.93 \times 10^{-2}$	$8.67 \times 10^{-1}$
ResNet18-GF	51.7	1.48	$4.08 \times 10^1$
PointNet	98.7	$8.64 \times 10^{-4}$	$8.45 \times 10^{-1}$

Table S1: OPA attack performance comparisons between ResNet18 and PointNet. ResNet18-GR indicates the attack within the range restriction of the greyscale value ( $0 \sim 255$ ), while ResNet18-GF indicates a purely numerical attack possibly with no physical significance (greyscale value less than 0 or greater than 255).

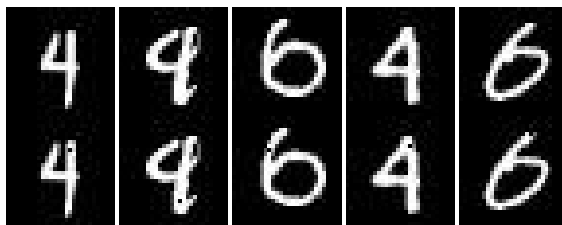


Figure S7: Successful attack examples of ResNet18-GR by OPA.

## 7.8 Visualization of the attribution distributions

As a supplementary of table 5, we demonstrate the complete pie diagrams of the attribution distributions of the aforementioned four pooling structures in S9.

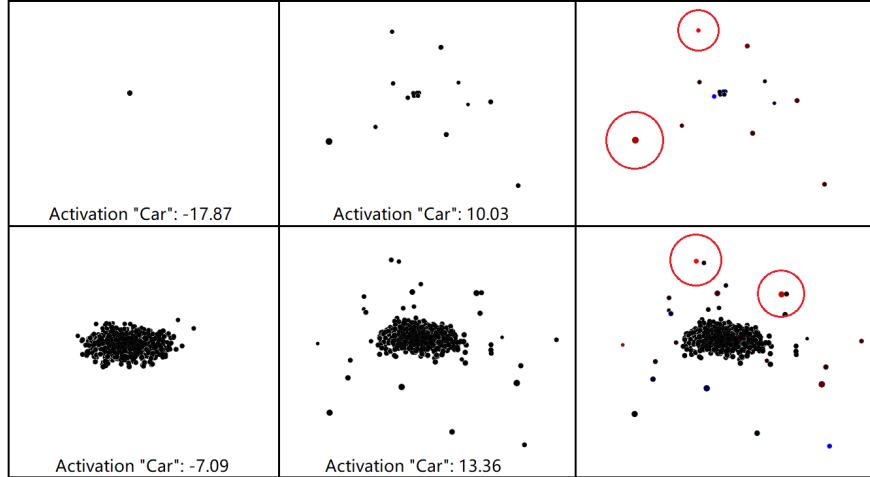


Figure S8: AM results initialized with zeros (the first row) and the point cluster generated by averaging all test data (the second row) respectively. The first, second and third columns demonstrate the initialized set of points, the AM output results after 1000 optimization steps and the salience map explanation of the corresponding output explained by IG, respectively. In the explanation, red points indicate the degree of positive attributions.

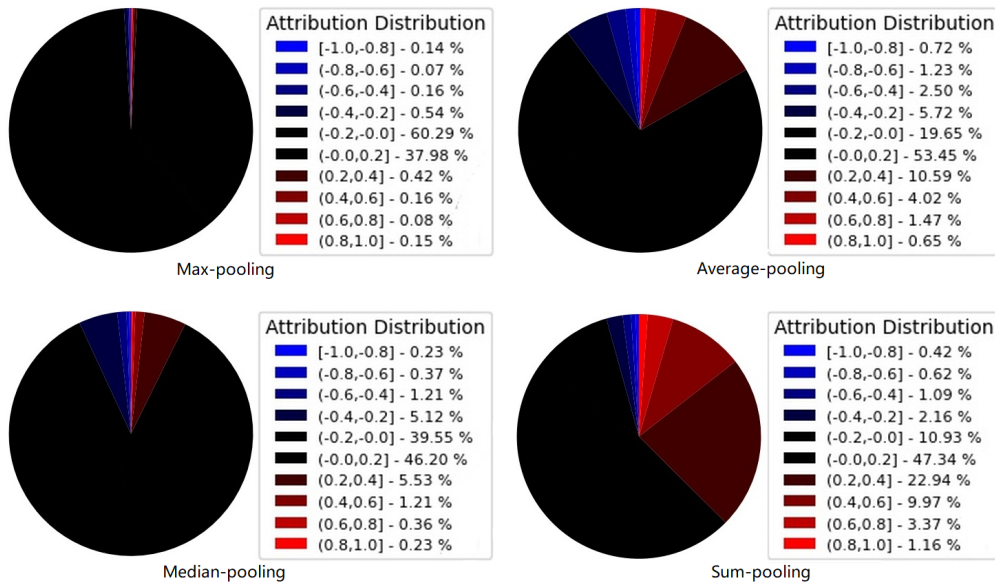


Figure S9: The distributions of attributed points of PointNet structured with max, average, median and sum-pooling layers as the global feature extraction layer respectively.